Special issue review article

NMR IN BIOMEDICINE

Received: 8 February 2012, Revised: 15 July 2012, Accepted: 1 October 2012, Published online in Wiley Online Library: 2012

(wileyonlinelibrary.com) DOI: 10.1002/nbm.2885

Cerebral blood volume MRI with intravascular superparamagnetic iron oxide nanoparticles

Seong-Gi Kim[a*,†], Noam Harel[b], Tao Jin[a], Tae Kim[a], Phil Lee[c] and Fuqiang Zhao[d]

The cerebral blood volume (CBV) is a crucial physiological indicator of tissue viability and vascular reactivity. Thus, noninvasive CBV mapping has been of great interest. For this, ultrasmall superparamagnetic iron oxide (USPIO) nanoparticles, including monocrystalline iron oxide nanoparticles, can be used as long-half-life, intravascular susceptibility agents of CBV MRI measurements. Moreover, CBV-weighted functional MRI (fMRI) with USPIO nanoparticles provides enhanced sensitivity, reduced large vessel contribution and improved spatial specificity relative to conventional blood oxygenation level-dependent fMRI, and measures a single physiological parameter that is easily interpretable. We review the physiochemical and magnetic properties, and pharmacokinetics, of USPIO nanoparticles in brief. We then extensively discuss quantifications of baseline CBV, vessel size index and functional CBV change. We also provide reviews of dose-dependent sensitivity, vascular filter function, specificity, characteristics and impulse response function of CBV fMRI. Examples of CBV fMRI specificity at the laminar and columnar resolution are provided. Finally, we briefly review the application of CBV measurements to functional and pharmacological studies in animals. Overall, the use of USPIO nanoparticles can determine baseline CBV and its changes induced by functional activity and pharmacological interventions. Copyright © 2012 John Wiley & Sons, Ltd.

Keywords: cerebral blood volume; iron oxide; contrast agent; fMRI; pharmacological MRI; monocrystalline iron oxide nanoparticle (MION); cortical columns; ultrasmall superparamagnetic iron oxide (USPIO) nanoparticles

INTRODUCTION

The cerebral blood volume (CBV) is a crucial physiological indicator of tissue viability and vascular reactivity, as CBV changes are linked directly to the regulation of blood flow under conditions of both normal and abnormal physiology. It is generally thought that dilation and constriction of the blood vessels are the major mechanisms that maintain cerebral blood flow (CBF) within an autoregulatory range, and adjust blood flow to perturbations, such as those induced by CO_2 changes and neural stimulation. Thus, the noninvasive measurement of neurovascular morphology and function is important.

In order to quantify CBV with MRI, an intravascular contrast agent can be utilized. When MR signal intensities are compared before and after the administration of the intravascular contrast agent, the difference is related to the blood volume (1–4). Most common approaches for human studies involve the injection of gadolinium diethylenetriaminepentaacetate (Gd-DTPA) into blood as a bolus (2), and imaging during the first pass of the contrast agent. The delivery of the agent into the brain vasculature is closely related to blood flow, and therefore the onset and peak times of MRI signal changes induced by the contrast agent vary depending on the blood flow characteristics of the tissue. However, a time integral of the MRI time course during the first pass is an index of CBV (5). As a result of the relatively short blood half-life of Gd-DTPA, its use for dynamic CBV studies is quite limited (3). Alternatively, iron oxide nanoparticles can be used as a blood pool agent (with a longer half-life than Gd-DTPA) for CBV imaging, and are generally classified into superparamagnetic iron oxide (SPIO) particles with a mean particle diameter of >50 nm, and ultrasmall superparamagnetic iron oxide (USPIO) particles with a smaller hydrodynamic diameter (6). With the same coating material (e.g. dextran), the former has a much shorter blood half-life than the latter (7). In order to use these iron oxide nanoparticles for CBV studies, an agent with a relatively long half-life is preferred in order to maintain the same concentration during the experimental duration. Thus, USPIO is the choice for functional CBV studies at steady state, whereas both USPIO and SPIO can be used for baseline CBV and angiographic imaging.

* *Correspondence to: S.-G. Kim, 3025 East Carson Street, McGowan Institute of Regenerative Medicine, Pittsburgh, PA 15023, USA. E-mail: kimsg@pitt.edu*

a *S.-G. Kim, T. Jin, T. Kim*
Neuroimaging Laboratory, Department of Radiology, University of Pittsburgh, PA, USA

b *N. Harel*
Center for Magnetic Resonance Research, Departments of Radiology and Neurosurgery, University of Minnesota, Minneapolis, MN, USA

c *P. Lee*
Hoglund Brain Imaging Center, Department of Molecular and Integrative Physiology, University of Kansas Medical Center, Kansas City, KS, USA

d *F. Zhao*
Imaging Department, Merck Research Laboratories, Merck Pharmaceuticals, West Point, PA, USA

† *The order of the authors is alphabetical except for the first author.*

Abbreviations used: *BOLD, blood oxygenation level-dependent; CBF, cerebral blood flow; CBV, cerebral blood volume; $CMRO_2$, cerebral metabolic rate of O_2 utilization; CNR, contrast-to-noise ratio; FLASH, fast low-angle shot; fMRI, functional MRI; Gd-DTPA, gadolinium diethylenetriaminepentaacetate; GE, gradient echo; IRF, impulse response function; IRON, increased relaxation for optimized neuroimaging; MION, monocrystalline iron oxide nanoparticle; rCBV, relative cerebral blood volume; SE, spin echo; SPIO, superparamagnetic iron oxide; USPIO, ultrasmall superparamagnetic iron oxide; VSI, vessel size index.*

The relationship between the susceptibility effect and tissue relaxation rate changes can be determined approximately by analytical solutions (8,9) and by Monte Carlo simulation (10–12). Iron oxide particles can be used to determine baseline CBV distribution and to provide insights into vessel size (13,14). In the late 1990s, long-half-life USPIO particles were used for functional studies (15–18), and Mandeville and colleagues later expanded the use of USPIO for functional and pharmacological MRI studies (19–22). This approach to the use of USPIO for functional studies is often referred to as 'increased relaxation for optimized neuroimaging (IRON)' (23), monocrystalline iron oxide nanoparticle (MION) (24), CBV-weighted or contrast agent-enhanced functional MRI (fMRI).

In this review, we describe the characteristics of USPIO, baseline CBV and vessel size measurements, functional CBV changes and application of CBV measurements to animal research. However, it is not our intention to review all CBV articles using USPIO, but rather to focus on principles and critical issues related to the quantification of CBV and its change. A recent review article of USPIO applications in animal studies can be found in Wu *et al.* (25). It should be emphasized that USPIO distributes into blood plasma; therefore, all quantitative measurements of baseline CBV need to consider hematocrit levels, whereas it is generally assumed that the hematocrit level does not change during relative CBV (rCBV) measurements. All of the following figures were obtained from the cat cortex in our laboratory.

PHYSIOCHEMICAL PROPERTIES AND PHAMACOKINETICS OF IRON OXIDE NANOPARTICLES

Iron oxide nanoparticles contain an iron oxide crystal core with a biodegradable coating. The core size of USPIO is 4–10 nm, and its structure can be a single crystal form (MION) (24). A hydrophilic polymer coating surrounding the iron oxide core is necessary to provide stability of the iron oxide in aqueous solution, and the common materials used are dextran and its derivatives (e.g. carboxylmethyl dextran). In addition to the hydrodynamic diameter, the coating material and surface charge will influence the blood half-life and biodistribution. Thus, the blood half-life of laboratory-made USPIO can vary between different batches and laboratories. In addition, the blood half-life is dependent on the species and dose. For example, commercially available Feraheme (ferumoxyl; AMAG Pharmaceuticals, Lexington, MA, USA) with a hydrodynamic diameter of 30 nm and a polyglucose sorbitol carboxymethylether coating has a blood half-life of approximately 15 h in humans (Feraheme instruction sheet) and >2 h in rats. In pigs, the blood half-life of dextran-coated MION was found to be approximately 50 min (26). In our studies, we found that the blood half-life is shorter in cats than in rats. In order to increase the blood half-life, we often infuse dextran solution to compete with dextran-coated USPIO. For most animal studies, a long half-life is preferred to maintain the same concentration during a long experimental time. Many review articles are available on the physiochemical properties, pharmacokinetics and biosafety of USPIO (6,27,28).

If a sterile and isotonic USPIO vial is obtained from commercial vendors (e.g. AMAG Pharmaceuticals), it should be directly injectable into the bloodstream. If USPIO is obtained from academic laboratories, its *in vivo* use may require further preparations by suspending it in phosphate-buffered saline and filtering through a sterile filter. If the USPIO batch is exposed to high temperatures, its particles may disintegrate and result in a shorter blood half-life.

USPIO nanoparticles are absorbed by the spleen, liver, bone marrow and lymph nodes (7), and are biodegradable. They are not assumed to have any long-term toxicity. Repeated intravenous injections of MION in monkeys (accumulated dose, 128 mg/kg) for over 1 year did not induce any noticeable side effects (29,30). However, repeated injections can increase blood iron levels, which can be removed by an iron chelating agent, such as deferoxamine, which binds free iron in the bloodstream and enhances its elimination.

MAGNETIC PROPERTIES OF IRON OXIDE NANOPARTICLES

Superparamagnetic properties occur when the crystal size is smaller than the ferromagnetic domains (~30 nm) (6). Furthermore, USPIO nanoparticles possess magnetism only when an external magnetic field is applied, and the induced magnetism is almost saturated at approximately 1 T [see Fig. 4 in ref. (24)] for MION. The magnetism of USPIO is dependent on the core size, so that different production batches may have different core sizes as well as magnetism. A change in proton relaxation rate (unit of s^{-1}) caused by iron oxide particles can be described as $\Delta R_1 = r_1 \times C$ and $\Delta R_2 = r_2 \times C$, where r_1 and r_2 are the relaxivity constants ($s^{-1}\,mM^{-1}$) and C is the iron concentration (mM). It should be noted that 1 mg Fe/mL is equivalent to 17.9 mM Fe. Relaxivity constants can be different in different magnetic fields (B_0) [see Fig. 2 in ref. (6)]. r_1 is robustly determined by a linear fitting of R_1 *versus* concentration, whereas R_2 *versus* concentration is slightly nonlinear at high iron concentrations (25). Thus, the Fe concentration can be determined from ΔR_1 of USPIO solution and r_1. The relaxivity constants of Feraheme are $r_1 = 38\,s^{-1}\,mM^{-1}$ and $r_2 = 83\,s^{-1}\,mM^{-1}$ at 20 MHz (0.47 T) (31). At 1.5 T, r_1 of MION is $13.9\,s^{-1}\,mM^{-1}$ (32). In our 9.4-T measurements, r_1 of MION was $1–1.7\,s^{-1}\,mM^{-1}$ in saline solution and blood plasma and r_2 was $70–110\,s^{-1}\,mM^{-1}$ in saline solution (33). r_1 decreases with B_0, whereas r_2 is almost independent of B_0. It should be noted that, in order to measure R_1 and R_2 of blood with USPIO, withdrawn blood can be centrifuged and only the plasma fraction retained in order to eliminate the precipitation of red blood cells during MR measurements.

In addition to changes in blood R_1 and R_2, USPIO induces the susceptibility effect, which can be used to quantify blood volume (see below). The susceptibility effect is closely related to the induced magnetism and Fe concentration. In order to determine the susceptibility effect of USPIO, two capillary tubes filled with saline (one oriented parallel to B_0 and the other perpendicular to B_0) are secured inside a cylinder containing a blood–USPIO mixture, and the frequency difference between the peaks originating from each of the capillaries is measured (14,34–36). The spectroscopic frequencies of water peaks originating from parallel- and perpendicular-oriented capillaries ($v_{||}$ and $v_{\perp}$, respectively) immersed in the withdrawn blood differ as a result of both hemoglobin in red blood cells and USPIO in plasma, and their separation can be expressed as $v_{||} - v_{\perp} = 2\pi\Delta\chi_{blood+agent}v_0$ (14,34,35), where $\Delta\chi_{blood+agent}$ is the susceptibility difference between the arterial blood containing USPIO and water, and v_0 is the spectrometer resonance frequency. All susceptibility

values are expressed in CGS units. As the susceptibility of plasma is similar to that of water (37), the susceptibility effect of the agent in plasma ($\Delta\chi_{agent}$) can be determined for each animal by the relationship, $\Delta\chi_{blood+agent} = Hct[Y\Delta\chi_{oxy} + (1 - Y)\Delta\chi_{deoxy}] + (1 - Hct)\Delta\chi_{agent}$, where Hct is the experimentally measured hematocrit, Y is the oxygenation level of blood, and $\Delta\chi_{oxy}$ and $\Delta\chi_{deoxy}$ are the susceptibility differences between fully oxygenated red blood cells and water and between fully deoxygenated red blood cells and water, respectively. As arterial blood is fully oxygenated, the $\Delta\chi_{deoxy}$ term can be ignored and the $\Delta\chi_{oxy}$ value is set equal to -0.026 ppm (38) to –0.035 ppm (35). The difference between reported $\Delta\chi_{oxy}$ values does not greatly impact the $\Delta\chi_{agent}$ calculation (e.g. the $\Delta\chi_{oxy}$ difference of 0.009 ppm, –0.026 *versus* –0.035 ppm, is much smaller than $\Delta\chi_{agent}$ of ~0.35 ppm). It should be noted that the difference between $\Delta\chi_{oxy}$ and $\Delta\chi_{deoxy}$ reported in the literature ranges between 0.18 ppm (38) and 0.27 ppm (35). Alternatively, in order to minimize the contribution of hemoglobin, plasma only can be used for susceptibility measurements. In our studies with 15 mg Fe/kg intravenous injection into rats, $\Delta\chi_{agent}$ of USPIO in plasma was 0.36 ppm (i.e. corresponding to the frequency shift of 904 Hz at 9.4 T) (36). As the induced magnetism is saturated at ~1 T, most animal studies performed between 4.7 and 11.7 T have similar frequency shifts induced by USPIO. In our studies, the frequency shift induced by USPIO at 9.4 T was found to be 1.1 times that at 4.7 T (33).

QUANTIFICATION OF BASELINE TOTAL BLOOD VOLUME

After USPIO is injected into the bloodstream, a steady-state condition is quickly achieved (7). Even when a small dose is used (e.g. 1 mg Fe/kg body weight), blood T_1 and T_2 are shortened significantly. In our 9.4-T rat studies (39), 1 mg Fe/kg body weight decreased arterial blood T_2 from 40 to 14 ms, and blood T_1 from 2.30 to 1.14 s. The USPIO intravenous injection dose of 1 mg Fe/kg body weight distributes to 60 mL volume/kg body weight, resulting in an USPIO concentration of ~0.017 mg Fe/mL blood (e.g. with a hematocrit level of 40%, an USPIO concentration of 0.028 mg/mL plasma is 0.50 mM). Thus, when a highly T_1-weighted pulse sequence with a short TE is used, especially at low B_0, blood vessels can be visualized because of the shortened T_1. This property has been exploited for angiography (31,40).

USPIO has been commonly used for CBV imaging in animals. The relationship between MION doses and R_2* is important to determine the appropriate dose of USPIO. For this, cats were used to determine the relationship between the tissue R_2* change and USPIO dose at 9.4 T (33). A dose of 2 mg Fe/kg of USPIO was repeatedly injected into the cat femoral vein until the total dose reached 10 mg/kg. After every injection, T_2*-weighted images with TEs of 6–40 ms were obtained at a steady-state condition (>2 min after the injection), and R_2* was calculated. The relationship between $\Delta R^*_{2,agent}$ of gray matter at 9.4 T and the USPIO injection dose was $\Delta R^*_{2,agent}\,(s^{-1}) = 5.49\,K$, where K is the USPIO dose (unit of mg Fe/kg body weight). This observation is consistent with results measured in the rat brain with USPIO: $\Delta R^*_{2,agent} = 5.80\,K$ at 4.7 T (18), $\Delta R^*_{2,agent} = 4.25\,K$ at 3 T (41) and $\Delta R^*_{2,agent} = 5.28\,K$ at 2.35 T (14). This shows that $\Delta R^*_{2,agent}$ induced by USPIO is similar at different magnetic fields. It should also be noted that the relationship between the USPIO dose and blood $\Delta R^*_{2,agent}$ is slightly nonlinear, unlike $\Delta R_{1,agent}$ (32).

To measure CBV with USPIO, it is preferable to inject a dose of 5–15 mg Fe/kg to create a large contrast between pre- and post-contrast images, and to obtain sufficient signal intensity of post-contrast T_2*-weighted images. The signal change induced by USPIO is directly related to the content of iron in a given pixel, and can be converted to $\Delta R^*_{2,agent}\,(s^{-1}) = \ln(S_{pre}/S_{post})/TE$, where S_{pre} and S_{post} are the signal intensities before and after USPIO. For example, fast low-angle shot (FLASH) images of cat brain with TE = 10 ms and a pixel resolution of $78 \times 78 \times 2000\ \mu m^3$ were acquired before and after a bolus injection of 12 mg Fe/kg MION (Fig. 1B, C). The calculated ΔR_2* map induced by MION (Fig. 1D) shows exquisite intracortical vessel patterns running into the cortex (42,43), low intensity in white matter and high intensity at the cortical surface. Interestingly, the middle part of the cortex has a slightly higher $\Delta R^*_{2,agent}$ band. This ΔR_2* value can be converted into CBV under an assumption of the static dephasing domain, as reported previously (8).

The static dephasing domain is commonly considered to be 1/(frequency shift induced by USPIO) $<< R_v^2/D$, where R_v is the vessel radius and $D = 0.8 \times 10^{-3}\ mm^2/s$ (14). Based on our studies, the frequency shift induced by a MION dose of 15 mg Fe/kg is ~900 Hz. The MION dose of 5 mg Fe/kg is expected to induce a frequency shift of ~300 Hz, equivalent to (1/frequency shift) = $1/(2\pi \times 300) = 5 \times 10^{-4}$, which, for a 2-μm-radius capillary, is much less than $R_v^2/D = (2 \times 10^{-3})^2/0.8 \times 10^{-3} = 5 \times 10^{-3}$. For the condition in which static dephasing is dominant, the change in the apparent transverse relaxation rate in tissue caused by the contrast agent, and in the absence of stimulation $(\Delta R^*_{2,agent})$ (8), can be described as:

$$\Delta R^*_{2,agent} = \frac{4}{3}\pi \cdot (1 - Hct) \cdot f_{CBV} \cdot \Delta\chi_{agent} \cdot \gamma B_0 \qquad [1]$$

where f_{CBV} is the whole blood volume fraction (mL blood/mL brain), which includes both plasma and blood cells, and γ is the gyromagnetic ratio, which is 2.675×10^8 rad/(s T). Baseline f_{CBV} (mL/mL) can be determined using Equation [1] from $\Delta R^*_{2,agent}$, and from Hct and $\Delta\chi_{agent}$ obtained from arterial blood. Assuming cortical Hct of 0.40 and $\Delta\chi_{agent}$ of 0.29 ppm [i.e. 0.36 ppm × (12/15)], $\Delta R^*_{2,agent}$ of $70\ s^{-1}$ in Fig. 1D (9.4 T) corresponds to f_{CBV} of 3.8 mL/100 mL. These f_{CBV} values are then converted to baseline CBV (mL/g) values by dividing by the blood density of 1.06 g/mL (44).

Generally, it is assumed that susceptibility-induced dephasing effects within a voxel are not influenced by neighboring voxels for CBV estimation. However, this assumption is not valid at a high spatial resolution (e.g. Fig. 1). In particular, baseline CBV determined from Equation [1] is overestimated when large vessels in neighboring voxels induce field gradients (see region near cortical surface in Figs 1 and 2E). An additional assumption is that the origin of the relaxation change is primarily from the extravascular compartment (8). The USPIO-induced signal change is on the order of approximately 50% in the extravasculature, whereas the intravascular blood signal before the MION injection is only a few per cent, which results in a very small error in CBV values.

A major advantage of USPIO over Gd-DTPA for CBV mapping is the longer blood half-life of USPIO. This allows the acquisition of high-resolution images of the entire brain and dynamic CBV measurements during interventions (see below) without concern for changes in contrast agent concentration. One major issue of USPIO is that it is not approved for human CBV studies, unlike Gd-DTPA. A detailed description of Gd-DTPA measurements can be found in Calamante (5). Compared with gadolinium

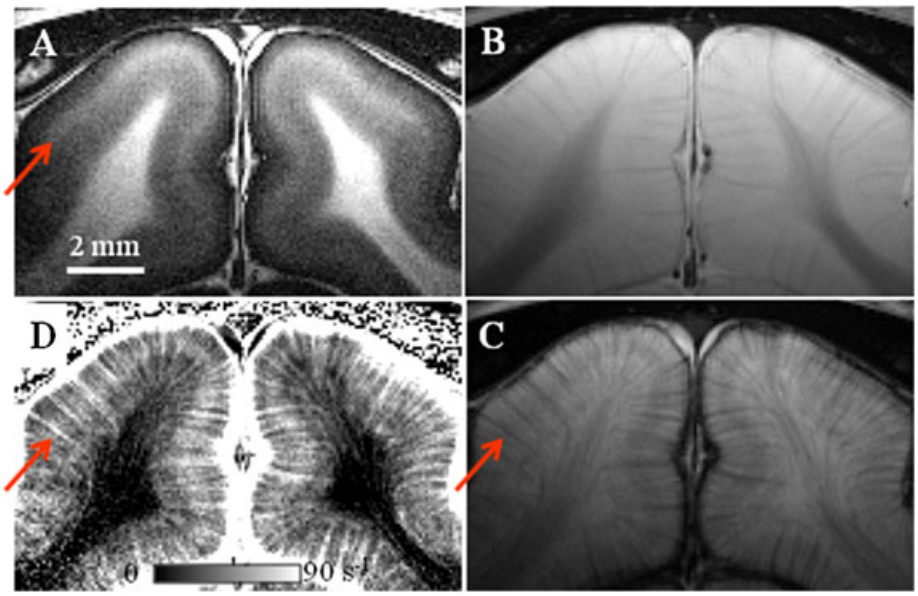

Figure 1. Determination of cerebral blood volume (CBV) distribution obtained from T_2*-weighted images of the cat brain with and without monocrystalline iron oxide nanoparticles (MION) (43). (A) A coronal slice of a T_1-weighted image was acquired using a four-segmented turbo-fast low-angle shot (FLASH) technique with a pixel resolution of 78 μm × 78 μm × 2 mm, flip angle of ~10°, TE = 5 ms, TR = 10 ms, intersegment delay of 4 s and an inversion time (TI) of 1.4 s at 9.4 T. White matter is hyperintense, and the red arrow indicates the myelin-rich stripe of Gennari, a prominent feature in layer 4, which is confirmed by histology (43). A T_2*-weighted image with TR = 40 ms, TE = 10 ms and intersegment delay of 100 ms was obtained before (B) and after (C) a bolus injection of 12 mg Fe/kg dextran-coated MION. (D) The baseline CBV-related $\Delta R^*_{2,agent}$ map was calculated from MR signal changes induced by MION (B *versus* C). The $\Delta R^*_{2,agent}$ value (gray bar) is linearly related to baseline CBV; CBV is highest at the surface of the cortex and lowest in white matter. Penetrating intracortical vessels can be easily visualized, and layer 4 (indicated by the red arrow) has a hyperintense band indicating high CBV.

chelates (about 1 nm in size), USPIO is more likely to remain in the bloodstream because of its larger hydrodynamic diameter, and thus is a better choice for CBV mapping in animals.

MAPPING BASELINE MICROVASCULAR VOLUME AND VESSEL SIZE INDEX (VSI)

The field gradient generated by blood iron oxides decreases by $(a/R_v)^2$, where a is the distance from the vessel to the region of interest and R_v is the vessel radius. During the TE typically chosen for MRI studies (e.g. ~50 ms), water molecules diffuse 10-20 μm [i.e. $(6 \times D \times TE)^{1/2} = (6 \times 0.8 \times 10^{-3} \times 0.05)^{1/2} = 0.015$ mm]. Thus, phase coherence of water spins near capillaries will be dynamically averaged over the steep field gradients produced by blood USPIO during TE, which cannot be recovered by a 180° radiofrequency pulse, whereas the dephasing effect around large veins can be refocused. Thus, the signal change in T_2*-weighted images is sensitive to vessels of all sizes, whereas that in T_2-weighted images is most sensitive to small vessels, where the diffusion contribution is dominant. The vessel size tuning of $\Delta R_{2,agent}$ is sensitive to the USPIO dose ($\Delta\chi_{agent}$) and TE; a higher dose and shorter TE result in tuning to a smaller vessel diameter (11,12). According to Monte Carlo simulations, the tuned vessel diameter is ~4 μm for a frequency shift of 160 Hz and TE of 100 ms (corresponding to 900 Hz and TE = 3.2 ms for the same diffusion distance over the same field difference) [see Fig. 2 in ref. (12)]. Both ΔR_2 and ΔR_2* increase with vessel diameter up to the tuned vessel diameter, but ΔR_2* is always larger than ΔR_2. Beyond the tuned diameter, ΔR_2* plateaus, whereas ΔR_2 decreases with vessel diameter [see Fig. 1 in ref. (12)]. Thus, ΔR_2* is sensitive to total CBV, whereas ΔR_2 is an index of microvascular CBV (13,14). Figure 2 shows ΔR_2* and ΔR_2 maps of the cat brain induced by 10 mg Fe/kg MION, obtained using echo planar imaging techniques with a pixel resolution of 156 μm 156 μm × 2 mm at 9.4 T (45). As shown in Fig. 1D, the surface of the cortex has very high $\Delta R^*_{2,agent}$ (Fig. 2B), but low $\Delta R^*_{2,agent}$ (Fig. 2C) values. Cortical profiles (Fig. 2E) show the highest $\Delta R^*_{2,agent}$ at the cortical surface because of large pial vessel contributions, and the highest $\Delta R_{2,agent}$ in the middle of the cortex, which is consistent with previous findings that middle cortical layers have the highest microvascular density (46). Interestingly, $\Delta R^*_{2,agent}$ decreases with cortical depth up to ~0.5 mm, which is probably a result of the extended dephasing effect from large surface vessels and the partial volume fraction of surface vessels within the slice thickness of 2 mm.

Baseline microvascular volume distribution can be obtained from $\Delta R_{2,agent}$ maps. As angiogenesis is of great interest, baseline CBV studies have often been performed in tumor models. Le Duc *et al.* (47) obtained $\Delta R_{2,agent}$ maps in normal and glioma-bearing rats, and found a high vessel density in the peripheral area and a low vessel density in the central area of the tumor. Wu *et al.* (48) measured microvascular volume distribution in mice with an injection of 30 mg Fe/kg at 9.4 T, and found that CBV in the cerebral cortex was higher in transgenic APP mice than in wild-type controls. Dunn *et al.* (49) used $\Delta R_{2,agent}$ in blood and tissue to determine microvascular volumes during angiogenesis, and compared them with those obtained using *in vitro* vascular fluorescence microscopy. The microvascular CBV values of control and vasodilated chronic hypoxic rats correlated well with those obtained from microvascular morphology. This indicates that $\Delta R_{2,agent}$ provides relative microvascular volume distribution and is a useful method to investigate angiogenesis.

Assuming that the susceptibility effect remains within a pixel, the pixel $\Delta R^*_{2,agent}/\Delta R_{2,agent}$ value provides microvessel size information (13,50). Tropres *et al.* (14) extended this idea to determine the VSI as:

NMR IN BIOMEDICINE

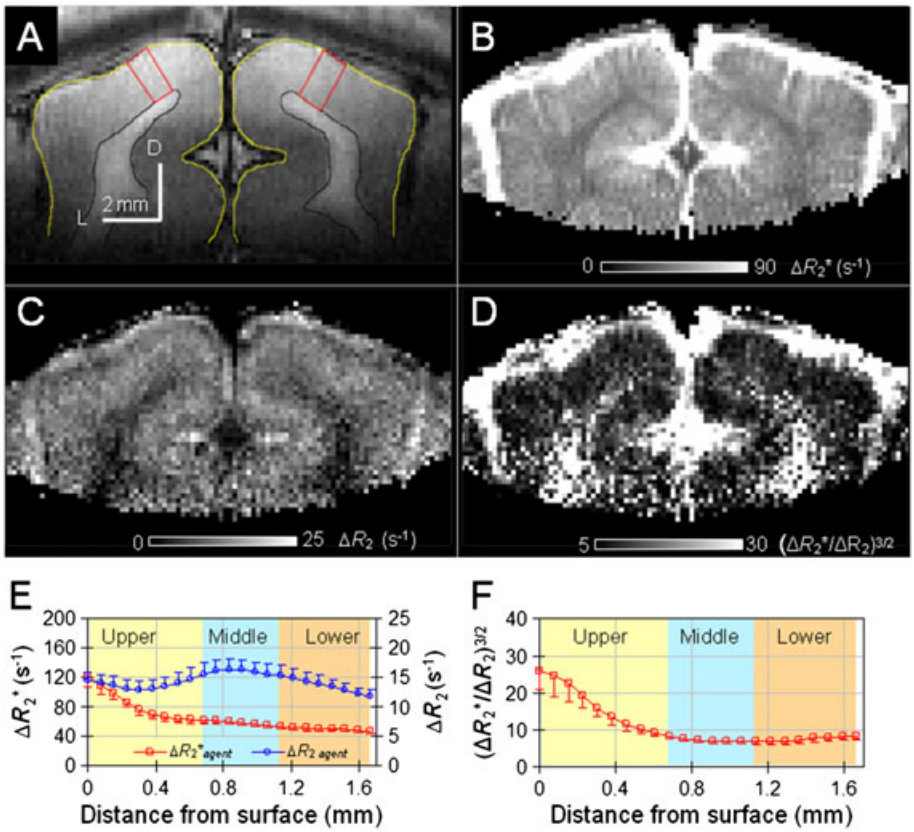

Figure 2. Baseline total and microvascular cerebral blood volume (CBV) and vessel size index (VSI) (45). (A) T_1-weighted anatomical image shows two quadrangular regions within the visual area 18 (outlined in red) for the subsequent cortical depth-dependent analysis. Each region was 700–900 μm wide and ~1.7 mm deep, extending from the surface of the cortex to the white matter. D, dorsal; L, lateral. Maps of $\Delta R^*_{2,\text{agent}}$ and $\Delta R_{2,\text{agent}}$ were obtained from gradient echo and spin echo MRI data with an injection of 10 mg Fe/kg MION at 9.4 T, and indicate distributions of total (B) and microvascular (C) CBV. Although an area with the largest total CBV is located near the surface of the cortex, the region with the highest microvascular CBV is located within the middle cortical layer. (D) The relative VSI generated by $(\Delta R^*_{2,\text{agent}}/\Delta R_{2,\text{agent}})^{3/2}$ shows a comparatively high ratio of large to small vessels at the cortical surface and within white matter. (E, F) One profile was generated for each animal from the quadrangular regions of interest in area 18 in (A), and the data were averaged across five animals. The surface of the cortex is at zero, with the cortical depth represented by increasing distances. An approximate location of the cortical layers was determined by the relative distances of the layers in area 18 (57), and is differentiated by colored bands; the middle cortical layer (approximately layer 4) is located in the region between 0.7 and 1.15 mm from the surface of the cortex. (E, F) Cortical depth profiles reflect the distribution of total CBV ($\Delta R^*_{2,\text{agent}}$; red squares) and microvascular-weighted CBV ($\Delta R_{2,\text{agent}}$; blue circles) signals (E) and VSI (F). The area with the largest total CBV is located at the surface of the cortex, whereas the region of highest microvascular CBV is located within the middle cortical layer (blue highlighted region).

$$\text{VSI} = 0.425\cdot\left(\frac{D}{\gamma B_0\cdot\Delta\chi_{\text{agent}}}\right)^{1/2}\cdot\left(\frac{\Delta R^*_{2,\text{agent}}}{\Delta R_{2,\text{agent}}}\right)^{3/2} \approx A\left(\frac{\Delta R^*_{2,\text{agent}}}{\Delta R_{2,\text{agent}}}\right)^{3/2} \quad [2]$$

where VSI (mm) is the weighted mean radius of the vessels, D (mm^2/s) is the diffusion coefficient and A is a constant. The VSI map is directly related to $(\Delta R^*_{2,\text{agent}}/\Delta R_{2,\text{agent}})^{3/2}$, and can provide insights into the composition of vessel sizes *in vivo*. Regions with larger VSI values indicate larger vessel sizes. Figure 2D, F shows the VSI map and cortical profile, respectively; the largest VSI is observed in the surface of the cortex, as expected. Assuming that USPIO remains within vessels, VSI has been used to examine the characteristics of angiogenesis (13,14,51). The exact weighted mean radius determined by VSI correlates well with *ex vivo* micro-computed tomography angiography and histological vessel measurements (52), but is six times larger in tumor and muscle than that obtained from optical microscopic imaging (53). Thus, VSI should be used as a relative measure of vessel diameter, rather than its absolute size. For example, Tropes *et al.* (51) determined that tumorous tissues had lower CBV, but larger VSI, compared with normal tissue, indicating that tumors contain less numerous, but larger sized vessels.

MAPPING QUANTITATIVE RELATIVE CBV CHANGE

USPIO is ideal for use for CBV-based fMRI studies because of its long blood half-life (15–18). Functional CBV-weighted signal changes accompany blood oxygenation level-dependent (BOLD) signal changes. Thus, the signal change induced by stimulation before and after USPIO needs to be examined further. The functional BOLD signal change before USPIO (ΔS_{pre}) is described as:

$$\Delta S_{\text{pre}} = S_0\cdot e^{-R^*_{2,\text{pre}}\text{TE}_{\text{pre}}}\left(-\text{TE}_{\text{pre}}\cdot\Delta R^*_{2,\text{BOLD}}\right) = S_{\text{pre}}\left(-\text{TE}_{\text{pre}}\cdot\Delta R^*_{2,\text{BOLD}}\right) \quad [3]$$

where $\Delta R^*_{2,\text{BOLD}}$ is linearly dependent on baseline venous CBV, B_0 and oxygenation level changes. The maximal ΔS_{pre} is achieved

at $R^*_{2,pre}\cdot TE_{pre} = 1.0$, and therefore the optimal TE is usually set to the tissue T_2*. Higher baseline venous CBV increases $R^*_{2,pre}$ and $\Delta R^*_{2,BOLD}$, but decreases baseline signal intensity (S_{pre}). Thus, at large vessel regions, the relative functional signal change ($\Delta S_{pre}/S_{pre}$) can be high, but the absolute functional BOLD signal change (ΔS_{pre}) decreases at higher fields because of increased $R^*_{2,pre}$ and reduced S_{pre}.

After USPIO is injected into blood, the baseline signal decreases and the functional signal change contains both CBV-induced USPIO susceptibility changes and deoxyhemoglobin-related BOLD signal changes (16,45,54). The post-agent functional signal change (ΔS_{post}) is described as:

$$\Delta S_{post} = S_0\cdot e^{-R^*_{2,post}\cdot TE_{post}}\left(-TE_{post}\cdot\Delta R^*_{2,BOLD} - TE_{post}\cdot C\cdot r_2^*\cdot\Delta CBV\right) \quad [4]$$

where $R^*_{2,post} = R^*_{2,pre} + \Delta R^*_{2,agent} = R^*_{2,pre} + C\cdot r_2^*\cdot CBV$, C is the USPIO blood concentration and r_2* is the relaxivity per millimole of USPIO (s^{-1}/mM). It should be noted that r_2* is almost independent of B_0. The relative functional signal change ($\Delta S_{post}/S_{post}$) has a BOLD contribution ($\Delta S_{pre}/S_{pre}$) and an absolute CBV change term. The BOLD contribution to $\Delta S_{post}/S_{post}$ can be corrected using pre-USPIO BOLD data. As C and r_2* are identical across pixels, the BOLD-corrected functional signal change is directly related to the absolute blood volume change. Then, the rCBV change ($\Delta CBV/CBV$) can be determined as:

$$\frac{\Delta CBV}{CBV} = \frac{(\Delta S_{pre}/S_{pre})/TE_{pre} - (\Delta S_{post}/S_{post})/TE_{post}}{\Delta R^*_{2,agent}} \quad [5]$$

At higher magnetic fields, the BOLD contribution is not negligible (55) and should be corrected in order to quantify the rCBV changes (16,45). The underlying assumption of the BOLD correction is that the BOLD signal change is identical between pre- and post-contrast agent conditions. This assumption is valid only when the intravascular BOLD contribution is minimal, because USPIO suppresses all intravascular signal contributions. If the intravascular BOLD contribution before USPIO injection is significant, the BOLD contribution to CBV-weighted fMRI using Equation [5] is overestimated; thus, the rCBV change ($\Delta CBV/CBV$) is slightly overestimated.

Examples of how to obtain $\Delta CBV/CBV$ are shown in Figs 3 and 4 (56). TE was set to 25 ms and 15 ms for the BOLD and CBV-weighted fMRI studies at 4.7 T, respectively. The baseline T_2* values of cat gray matter were ~51 ms and ~21 ms before and after the 7-mg/kg MION injection, respectively. During a visual stimulation period, the largest BOLD signal changes

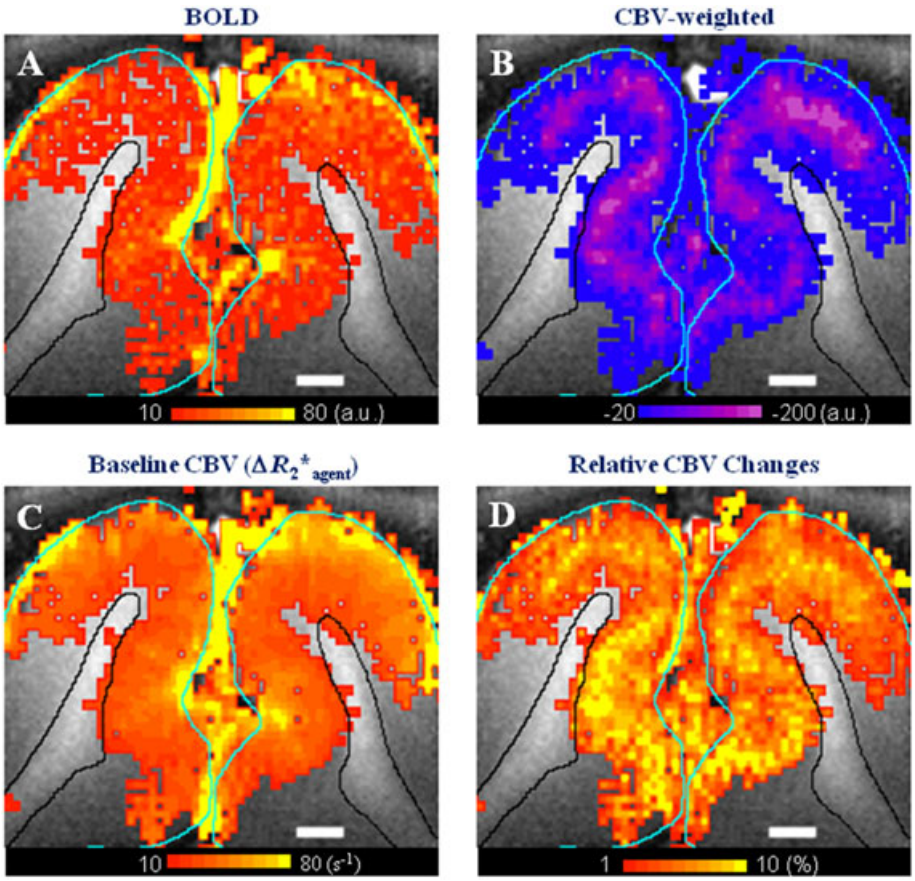

Figure 3. Blood oxygenation level-dependent (BOLD) contribution to cerebral blood volume (CBV)-weighted functional MRI (fMRI) signal. (A, B) Absolute functional signal changes (ΔS maps) of BOLD and CBV-weighted signals, respectively, obtained with 7 mg Fe/kg at 4.7 T. Purple/blue color (B) indicates a decrease in MRI signal. Maximum BOLD changes responding to visual stimulation occur in large vessel regions, whereas the largest monocrystalline iron oxide nanoparticle (MION) signal changes occur in the middle cortical areas. Changes in R_2* ($\Delta R^*_{2,agent}$) induced by contrast agents (C) are linearly related to the baseline CBV. (D) Calculated relative CBV map with the correction of the BOLD contribution. The pattern of increased CBV in the middle layers was preserved. The green contour indicates the cortical surface and the black contour indicates white matter. Scale bar, 1 mm.

NMR IN BIOMEDICINE

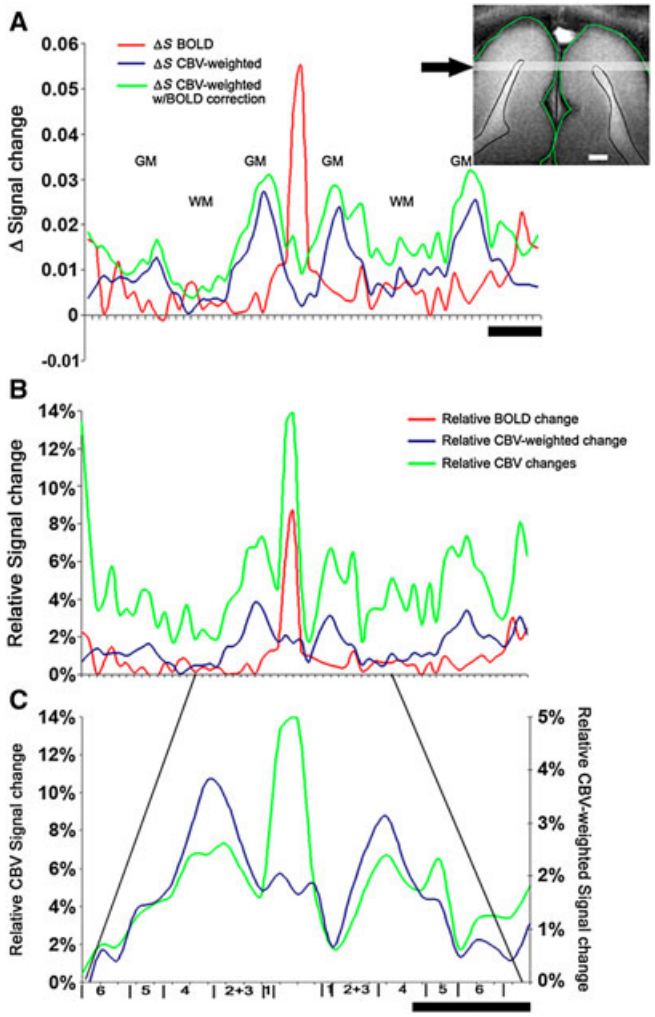

Figure 4. Laminar distribution of blood oxygenation level-dependent (BOLD), cerebral blood volume (CBV)-weighted and relative CBV (rCBV) signal changes (56). Signal profiles of Fig. 3 data were plotted across the cortical layers of the lateral gyrus, indicated by an arrow on the anatomical image. For comparison, all signals were plotted as the positive change. (A) Absolute signal changes of BOLD, CBV-weighted and CBV-weighted with BOLD correction. (B) Relative signal changes (%) of BOLD, CBV-weighted and CBV with BOLD correction. (C) An enlarged segment of (B) corresponding to the medial section of both lateral gyri. Schematic boundaries between cortical layers were superimposed. GM, gray matter; WM, white matter. Scale bar, 1 mm.

(yellow) occurred mainly in the upper layers/cortical surface, whereas smaller signal changes occurred in deeper layers (Fig. 3A). Following MION injection, the MRI signal decreased during neural stimulation, indicating an increase in CBV (Fig. 3B). The CBV-weighted signal was confined to the primary visual areas and closely followed the gray matter contour. In contrast with the BOLD signals, the maximum CBV-weighted signals were centered over the gray matter, whereas a significantly smaller signal was detected at the cortical surface. However, the CBV-weighted signal is dependent on the dose of MION and CBV changes, as well as BOLD contributions. Basal CBV levels were obtained by measuring ΔR_2^* induced by MION (Fig. 3C). Although CBV-weighted fMRI signal changes are negligible in large vessel areas (Fig. 3B), quantitative rCBV changes (rCBV map) are significant (Fig. 3D). More importantly, larger stimulation-induced rCBV changes take place at the center of the cortical gray matter. To better exemplify the properties of the stimulus-induced functional signal changes, their profiles were plotted across cortical layers (Fig. 4). To correlate the functional maps with the underlying cortical laminar structures, schematic boundaries between cortical layers, based on the literature (57) and previous histological studies (43,58), were superimposed (Fig. 4C). Both rCBV and CBV-weighted signals exhibit elevated signals at middle cortical layers, with smaller changes at upper surface vessels and white matter regions.

As mentioned in the previous section on Mapping Baseline Microvascular Volume and Vessel Size Index (VSI), spin echo (SE) and VSI fMRI approaches can be used to characterize the size of vessels that are functionally responding. To obtain an insight into the hemodynamic regulation, we can assume that baseline $CBV_{total} = CBV_{micro} + CBV_{macro}$, where CBV_{micro} and CBV_{macro} are the micro- and macrovascular volumes, respectively. As a portion of small arterioles and venules can contribute to these SE measurements, the boundary between micro- and macro-vessels is not well defined. Changes in relative total and microvascular volumes were measured, where stimulation-induced $\Delta rCBV_{total} = (\Delta CBV_{micro} + \Delta CBV_{macro})/(CBV_{micro} + CBV_{macro})$ and $\Delta rCBV_{micro} = \Delta CBV_{micro}/CBV_{micro}$. If a change in relatively large vessels is dominant, $\Delta rCBV_{micro}$ (measured by SE fMRI) should be very small relative to $\Delta rCBV_{total}$ [measured by gradient echo (GE) fMRI]. If a change in the capillary volume is dominant, $\Delta rCBV_{micro}$ should be larger than $\Delta rCBV_{total}$. It should be noted that SE measurements underestimate the true microvascular volume change because the sensitivity of vessels larger than the tuned diameter decreases. We reported a 5.6% $\Delta rCBV_{micro}$ and a 10% $\Delta rCBV_{total}$ in the middle of the cortex (45), which indicates that most responding vessels are larger than the tuned vessel diameter (capillaries). Similarly, as VSI provides an index of a weighted vessel size, comparison of VSI between the baseline and functional conditions will provide information on the responding vessel sizes. Zhao *et al.* (45) showed an average ratio of stimulation to baseline VSI values (relative VSI) in the middle of the cortex of 2.80. In other words, if the weighted vessel radius was 2 μm in the middle cortex, the corresponding weighted vessel radius responding to stimulation would be ~6 μm. This indicates that dilated vessels responding to neural stimulation are larger than capillaries.

Similar studies were performed in rats by Mandeville *et al.* (59). In their studies, higher baseline $(\Delta R^*_{2,agent}/\Delta R_{2,agent})^{3/2}$ and lower $\Delta rCBV_{total}/\Delta rCBV_{micro}$, resulting in a higher baseline VSI and almost constant functional VSI. This indicates that the large vessel responses are not dominant, which is similar to the conclusion made by Zhao *et al.* (45). However, functional VSI is much less than baseline VSI, which is consistent with the results at the cortical surface in Zhao *et al.* (45), but not with the results within the cortex. When $\Delta S_{post}/S_{post}$ is calculated from SE fMRI after an USPIO injection, it relates to an absolute change in microvascular CBV, which is always less than the total CBV change. As most vessels are larger than the tuned diameter, its diameter change subquadratically contributes to SE measurements [see sensitivity profile in ref. (12)]. The microvascular CBV change measured by SE fMRI with USPIO underestimates the true change (59). Thus, SE fMRI should not be used for the accurate determination of the absolute CBV response.

SENSITIVITY AND SPECIFICITY OF CBV-WEIGHTED VERSUS BOLD FMRI

The functional sensitivity of the CBV-weighted fMRI signal [Equation [4]] is closely dependent on the dose of USPIO, baseline CBV and BOLD contamination, as well as stimulus duration (30). As the BOLD contrast increases with B_0, and the magnetization of iron oxides is saturated above ~1.0 T (24), the stimulation-induced signal of CBV-weighted fMRI decreases at higher B_0 because of the counteractive effect of BOLD relative to the CBV response. Generally, with lower B_0, the functional sensitivity gain over conventional BOLD fMRI increases. B_0-dependent sensitivity properties were investigated by Mandeville *et al.* (17).

The reported sensitivity values were measured under a steady-state condition. The CBV-weighted fMRI sensitivity is approximately six times greater than the GE BOLD fMRI signal at 2 T (12 mg Fe/kg, TE = 25 ms) and 1.5–2 times greater at 4.7 T (16 mg/kg, TE = 25 ms) in rats (17), and three times greater at 3 T in monkeys (8–10 mg/kg, 20 ms for MION *versus* 30 ms for BOLD) (29,30). At 7 T, 15–20 mg/kg USPIO improves the functional contrast-to-noise ratio (CNR) by 70% in rats compared with BOLD (TE = 14 ms for BOLD and USPIO) (60). At 9.4 T, the improvement in CNR is 1.2–1.5 times in the cat visual cortex (MION of 10 mg/kg, TE of 10–15 ms for CBV-weighted fMRI *versus* TE of 20 ms for BOLD fMRI) (33). Mandeville *et al.* (21) reported that CNR in CBV-weighted GE fMRI with 28 mg Fe/kg and TE of 5 ms improved twofold compared with GE BOLD with TE of 10 ms in the rat brain during cocaine stimulation. Very recently, Qiu *et al.* (61) used USPIO for 3-T human fMRI studies, showing two to three times CNR improvement over GE BOLD in the human visual cortex using a dose of 7 mg/kg. To maximize the sensitivity gain, TE_{post} should be set to $1/R^*_{2,post}$. The BOLD contribution to CBV-weighted fMRI could also be minimized by using a short TE value.

The sensitivity of CBV-weighted fMRI [Equation [4]] also depends on the baseline CBV because the baseline signal intensity is related to $\exp(-TE_{post} \cdot C \cdot r_2^* \cdot CBV)$. This baseline CBV-dependent functional sensitivity was examined by Mandeville and Marota (19). When the USPIO dose and TE are optimized for one baseline CBV value, namely CBV_{ref}, ΔS_{post} is modulated by $\exp(-CBV/CBV_{ref})$; thus, regions with a large baseline CBV have decreased functional sensitivity. This baseline CBV-dependent function is referred to as a vascular filter (19).

What is the consequence of the vascular filter on CBV-weighted fMRI? Regions with large vessels lose their baseline signals more rapidly than regions with cortical microvessels, thus less absolute signal changes are induced by the same absolute CBV change. This phenomenon is similar to large vessel regions at long TEs or at very high fields; even if the relative percentage change ($TE\Delta R^*_{2,BOLD}$) is quite high, the absolute signal change (ΔS_{pre}) is low because of the low baseline signal intensity. This mechanism has been proposed to be a major reason for the improvement in the spatial localization (19). In addition, large BOLD contributions at vessel areas reduce the CBV-weighted signal change. Thus, activation foci in CBV-weighted images obtained as statistical values (or absolute intensities) can shift to deeper cortical areas compared with BOLD fMRI (Fig. 3A *versus* Fig. 3B and 4A). Supporting findings have been reported in the rat somatosensory cortex (19) and the monkey visual cortex (62).

The improved spatial localization of CBV-weighted fMRI may be a result of true physiological responses, rather than just the vascular filter function. This hypothesis can be tested in two ways: (i) by quantifying the rCBV change and comparing it with the CBV-weighted response; and (ii) by comparing measurements with different filter functions. First, to remove baseline signal dependences from the activation maps, percentage signal changes from baseline ($\Delta S/S$) are calculated (see Fig. 4B), and then the BOLD contribution is corrected. Peak positions in CBV-weighted ΔS (blue trace in Fig. 4A), CBV-weighted $\Delta S/S$ (blue trace in Fig. 4B) and rCBV changes (green trace in Fig. 4B) within the cortex remain the same. Second, SE *versus* GE fMRI with USPIO shows peak responses in the middle of the cortex and independence from the vascular filter functions (45). Third, three MION doses of 5, 10 and 15 mg Fe/kg were used at TE = 10 ms at 9.4 T. The peak positions of the CBV-weighted fMRI response remain the same with different MION doses (see Fig. 5). A similar finding was reported by Keilhotz *et al.* (63), in which spin-echo fMRI was performed on the rat somatosensory cortex with 10, 20 and 30 mg Fe/kg at 11.7 T. The spatial peak of the percentage signal changes in CBV-weighted fMRI was invariant of the dose of MION and pulse

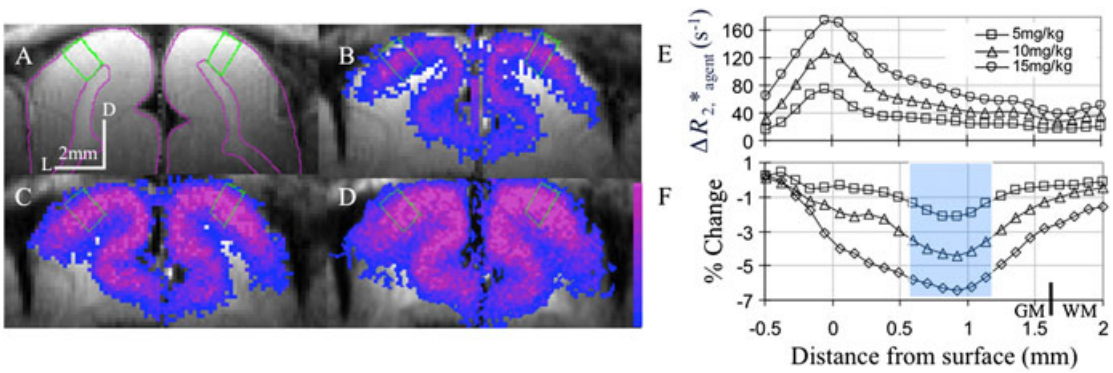

Figure 5. Dose-dependent cerebral blood volume (CBV)-weighted functional MRI (fMRI) changes. As the dose of iron can modulate neural activity-induced signal changes, CBV-weighted fMRI signals were measured with 5, 10 and 15 mg Fe/kg using gradient echo data acquisition at 9.4 T. The anatomic echo planar image (A) delineates gray matter (GM) from white matter (WM). For better visualization, lateral gyri are shown as pink contours in both hemispheres. In order to show the effects of monocrystalline iron oxide nanoparticle (MION) doses on baseline $\Delta R^*_{2,agent}$ (s^{-1}) and CBV-weighted fMRI (%), cortical profiles were obtained (E, F) from the green regions of interest in (A). When the dose of MION was increased from 5 to 15 mg/kg, a steeper $\Delta R^*_{2,agent}$ profile from the cortical surface was created, but the functional peak position was similar. Blue highlighted region in (F) indicates layer 4.

sequence, indicating that the improved spatial localization of CBV-weighted fMRI is a result of true physiological responses.

SENSITIVITY OF CBV-WEIGHTED FMRI *VERSUS* DOSE OF USPIO

The choice of USPIO dose is critical to maximize the functional sensitivity. Two conditions can be considered: (i) $TE_{post} = TE_{pre} = 1/R^*_{2,pre}$; and (ii) $TE_{post} < TE_{pre}$. For condition (i), the USPIO dose is optimal when the baseline signal decreases to e^{-1} of the pre-contrast intensity [Fig. 5a in ref. (19)] at $TE_{post} \cdot C \cdot r^*_2 \cdot CBV = TE_{post} \cdot \Delta R^*_{2,agent} = 1.0$. For condition (ii), if TE_{post} is set to as short as possible, the USPIO dose is determined by $R^*_{2,post} = 1/TE_{post}$ [see Fig. 5b in ref. (19)]. The sensitivity gain of condition (ii) relative to condition (i) is $\exp(-TE_{post}/TE_{pre})$ [Fig. 5b in ref. (19)]. Most CBV-weighted fMRI studies use the latter condition.

During long experimental times, the USPIO blood concentration decreases and, consequently, functional CBV-weighted $\Delta S/S$ similarly decreases. Figure 6 shows time courses of CBV-weighted fMRI signals more than 2 h after the administration of 10 mg Fe/kg MION (64). For this specific and early application of MION in our laboratory, additional dextran solution (to increase the blood half-life of dextran-coated MION) was not infused, unlike the remainder of our cat experiments. Positive BOLD responses and negative CBV-weighted responses were consistently obtained from area 18 of the cat visual cortex. As the MION concentration in blood decreased by clearance processes, the CBV contrast diminished accordingly. To remove iron concentration-dependent variations, an index of baseline Fe concentration ($\Delta R^*_{2,agent}$) should be measured, and used for the determination of the rCBV change [see Equation [5]]. Thus, baseline $\Delta R^*_{2,agent}$ at each time course was calculated from baseline data. When rCBV changes were calculated with BOLD correction (Fig. 6B), CBV time courses were similar. In particular, when the concentration of MION in the blood is low, the BOLD correction is essential to determine functional rCBV changes.

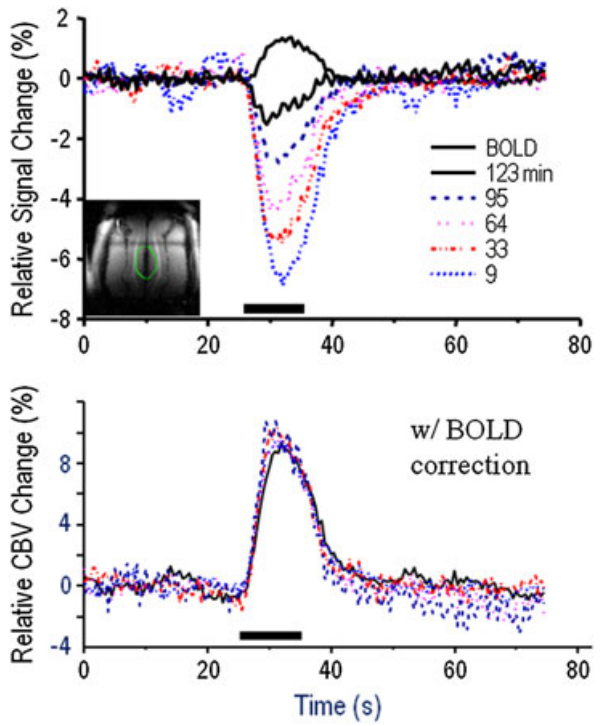

Figure 6. Experimental time-dependent functional MRI (fMRI) and relative cerebral blood volume (rCBV) time courses during the decay of monocrystalline iron oxide nanoparticle (MION) contents (89). fMRI responses of the cat visual cortex induced by visual stimulation were performed from the green region of interest (inset image) before and after an injection of 10 mg/kg MION at 4.7 T (TE = 20 ms, TR = 0.5 s). MION was removed more quickly from blood when an additional dextran solution was not infused in cats (note that all other cat studies used additional dextran solution). The negative change in (A) indicates that the CBV-weighted response is much larger than the positive BOLD contribution. rCBV changes were calculated using BOLD and MION time courses with Equation [5], showing that the time-dependent variations in CBV-weighted fMRI can be removed. Horizontal bars underneath the time courses indicate the stimulus duration.

CHARACTERIZATIONS OF CBV-WEIGHTED FUNCTIONAL RESPONSES

Evoked CBV changes have an initial fast increase, followed by slow increases during long stimulation (65,66). It should be noted that, although functional CBV-weighted changes are negative, the absolute changes are used for comparison with BOLD responses. The impulse response function (IRF) of CBV-weighted fMRI differs from that of BOLD fMRI. Silva *et al.* (66) measured IRF in the rat somatosensory cortex at 11.7 T, and found that the CBV response started and peaked ~0.5 s earlier than the BOLD response. Leite *et al.* (30) systematically determined IRFs of CBV-weighted and BOLD fMRI of visual cortex in awake monkey at 3 T. When a 4-s stimulation was used, both CBV-weighted and BOLD responses peaked at a similar time, but the CBV-weighted signal returned to baseline after the stimulus offset more slowly relative to BOLD fMRI. However, when the stimulation duration was 60 s, the first-order time constants of the responses were 4.5 s for BOLD and 13.5 s for CBV-weighted fMRI. This indicates that a long stimulation duration increases the functional sensitivity of CBV-weighted fMRI relative to BOLD fMRI (30), and that the CBV-weighted signal responding to long stimulation cannot be explained by a time-invariant linearity function with the IRF obtained from short stimulation (67).

As CBV-weighted fMRI provides higher sensitivity than BOLD fMRI, it can be used for high-resolution fMRI studies in animals. In order to examine time-dependent CBV-weighted fMRI, CBV-weighted fMRI images were obtained at 2-s intervals following each stimulation onset (see Fig. 7). The CBV change initially shows significant radial vessel contributions (see Fig. 7A, B), following dominant responses in the middle of the cortex (see Fig. 7D), indicating that a later response is highly specific (68). For CBV-weighted fMRI with a resolution of $98 \times 98 \times 1000\ \mu m^3$ and 6 mg Fe/kg, Palmer *et al.* (69) successfully separated localized functional sites induced by forepaw and hindpaw stimulation in α-chloralose anesthetized rats at 4.7 T. In CBV fMRI experiments with a resolution of $156 \times 156 \times 2000\ \mu m^3$ at 3 T after 12 mg Fe/kg injection (70), rat whisker barrel cortex showed the highest response to whisker stimulation in layer 4, similar to c-Fos expression maps. These studies indicate that the functional CBV response is quite specific to small functional structures.

The specificity of the CBV response at a cortical columnar scale has been examined by our laboratory (56,71,72). The CBV-weighted fMRI approach with 10 mg Fe/kg and a resolution

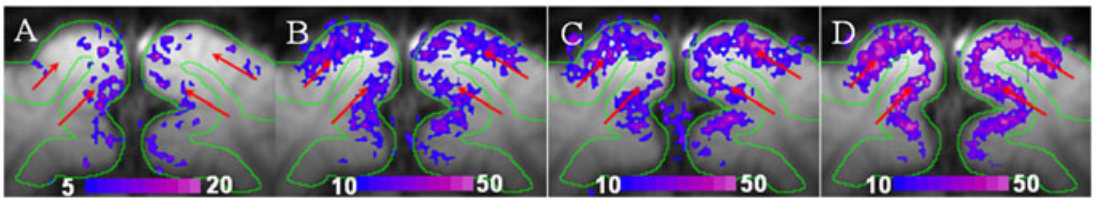

Figure 7. Time-dependent functional maps of cerebral blood volume (CBV)-weighted functional MRI (fMRI) signals. CBV-weighted fMRI of the cat visual cortex was obtained with a resolution of $156 \times 156 \times 2000\,\mu m^3$ during a 10-s visual stimulation after a 10-mg/kg injection at 9.4 T. The functional *t*-value maps were calculated from 2 to 3 s (A), 3 to 4 s (B), 4 to 5 s (C) and 9 to 10 s (D) after the stimulation onset. A contiguous cluster size of three active pixels was imposed. The *t*-value threshold was $t > 5$ for (A) and was adjusted between 10 and 13.5 to provide a similar number of activated pixels for (B–D). The middle cortical layer is indicated by red arrows. Clearly, the later CBV response is more specific to the middle of the cortex. Blue/purple bar, *t* value.

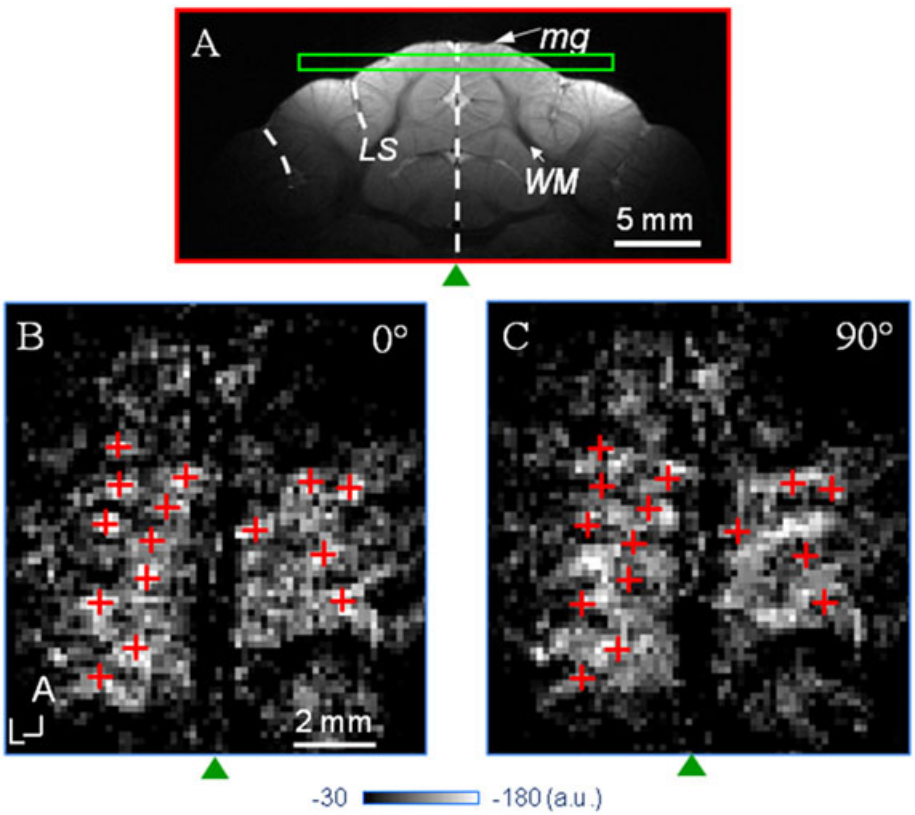

Figure 8. Cerebral blood volume (CBV)-weighted functional MRI (fMRI) responses at columnar resolution obtained with two orthogonal stimulation orientations (71). (A) Images with an in-plane resolution of $156 \times 156\,\mu m^2$ were obtained from a 1-mm-thick slice parallel to the surface of the cortex during moving grating stimulation of either 0° or 90° orientation at 9.4 T. Raw gray-scale functional maps were initially determined by the subtraction of images obtained during 0° (B) or 90° (C) stimulation from pre-stimulus control images without thresholding. The bright pixels in these single-condition maps have the largest (negative) signal changes induced by stimulation. The center of each patch on the 0° map (B) is marked with a red '+' sign; these symbols were then overlaid on the 90° map (C). A, anterior; au, arbitrary unit; LS, lateral sulcus; M, medial; mg, marginal gyrus; WM, white matter; green arrowheads, midline.

of $156 \times 156 \times 1000\,\mu m^3$ was applied to map cat orientation columns at 9.4 T (71,72), which could not be obtained with conventional BOLD fMRI under the same animal model and experimental conditions (73). Figure 8 shows the subtraction maps of 0° and 90° stimulation. Clearly, activations responding to 0° stimulation (red crosses) are not in the same location as those of 90° stimulation. Regions of large CBV changes responding to two orthogonal orientation gratings were highly complementary, indicating that parenchymal CBV responses are quite specific to neural active sites in a steady-state condition (71,72). To further examine functional CBV responses at the columnar and laminar level, we employed the well-established ocular dominance column model (74). Following 7 mg Fe/kg administration, functional CBV-weighted images were acquired with a resolution of $156 \times 156 \times 2000\,\mu m^3$ and TE of 15 ms at 4.7 T (56). Figure 9 shows statistical maps for binocular and monocular CBV-weighted activation maps from two cats to demonstrate the consistency of our findings. During binocular stimulation, a more homogeneous pattern of increased CBV was observed along the middle cortical layers. On the contrary, during monocular stimulation, local patches of increased CBV-weighted signals were observed. In all cases, the contralateral hemisphere to the stimulated eye exhibited a larger number of activated pixels ($58.1 \pm 3.7\%$; $n = 5$). Patches of localized increases in blood volume were arranged in an orderly fashion across the middle layers throughout the primary visual cortex. The mean distance between

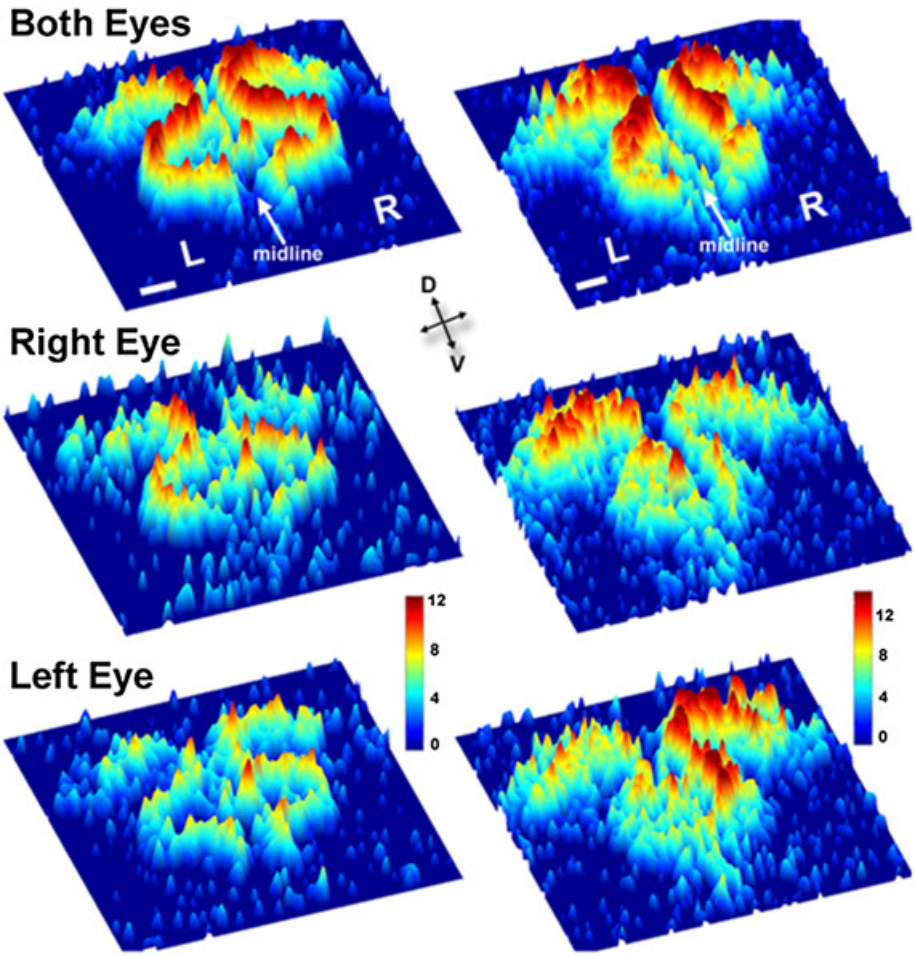

Figure 9. Cerebral blood volume (CBV)-weighted functional maps induced by binocular and monocular visual stimulation (56). CBV-weighted functional MRI (fMRI) of cat visual cortex was obtained with 7 mg Fe/kg monocrystalline iron oxide nanoparticles (MION) at 4.7 T. Two examples of statistical maps are shown for binocular (top row) and monocular CBV-weighted activation maps (middle and lower rows, right and left eyes, respectively). During binocular stimulation, a more homogeneous pattern of increased CBV was seen along the middle cortical layers. On the contrary, in monocular stimulation, local patches of increased CBV-weighted signals were observed. D, dorsal; L, left hemisphere; R, right hemisphere; V, ventral; color bar, *t* values. Scale bar, 1 mm.

the centers of adjacent peaks at the medial parts of the lateral gyrus (area 17) was 0.57 ± 0.14 mm ($n = 4$ cats, total of 124 pairs). Territories dominated by the left eye and the right eye clearly alternated. These results indicate that CBV is regulated at a columnar and laminar level.

APPLICATION TO NEUROVASCULAR AND NEUROSCIENCE RESEARCH

The use of USPIO is ideal to determine dynamic CBV changes induced by ischemia and global stimulation. The earliest applications were to measure CBV changes during ischemia (75–77). Many vascular reactivity studies followed, whereby breathing gas was manipulated (78–81).

USPIO was applied to obtain neural activation-induced fMRI (16–18,69). Although USPIO was used for preliminary human fMRI studies (61), it is currently not approved as a blood pool agent for humans. Thus, we focus our literature review on animal studies. A common application of CBV-weighted fMRI is to determine the underlying BOLD mechanism and to enhance fMRI sensitivity in animals. As BOLD fMRI is related to a combination of CBF, cerebral metabolic rate of O_2 utilization ($CMRO_2$) and CBV responses, measurements of the CBV response can help to determine the CBV contribution to BOLD (16) and the $CMRO_2$ change (82–86). To determine the $CMRO_2$ change with BOLD biophysical models, it is crucial to determine the relationship between $\Delta CBF/CBF$ and $\Delta CBV/CBV$ (87), which can be expressed as $\Delta CBV/CBV = (\Delta CBF/CBF)^{\alpha}$, where α is a constant. Measured α values are dependent on brain regions and time after the stimulus onset (68,84,88). At a steady-state condition, the α values obtained during neural stimulation are 0.43 (84) and 0.19–0.23 (88) in the rat somatosensory cortex and ~0.2 in the cat visual cortex (68). In both rat studies [3 T, 12 mg Fe/kg, TE = 27.2 ms for ref. (84) and 7 T, 8 mg Fe/kg, TE = 20 ms for ref. (88)], the BOLD contribution to CBV-weighted fMRI was not corrected, and thus the CBV change was slightly underestimated. An important point is that the BOLD signal is directly related to the venous CBV change, not the total CBV change. fMRI with USPIO measures the total CBV change, which is much larger than the venous CBV change (36,43,89,90). Thus, when the total CBV is used, the contribution of CBV to BOLD signals is overestimated and, consequently, the $CMRO_2$ change is underestimated. To separate the total CBV into arterial and

venous CBV, arterial CBV measurement techniques (39,91,92) can be combined with USPIO studies.

As the use of USPIO can enhance functional sensitivity, it is often employed for monkey fMRI studies (29,30,93). In nonhuman primate studies, human MR scanners are often used and experimental time is limited. Thus, an increase in the functional sensitivity is of high priority. Vanduffel *et al.* (29), Durand *et al.* (94) and Tsao et al. (95) and their colleagues routinely use USPIO for monkey fMRI studies. These neuroscience applications are beyond the scope of this review article. For rodent fMRI studies, as high-field animal MRI systems are becoming widely available and BOLD fMRI can be used, CBV-weighted fMRI is less frequently used for neuroscience research relative to its use in nonhuman primate studies. Mueggler *et al.* (96) used USPIO to image functional activity in transgenic mice, and Zhao *et al.* (97,98) used USPIO to image pain responses in the spinal cord and cortex.

USPIO has been used for pharmacological MRI, which investigates hemodynamic responses induced by drugs, because of its high sensitivity and its measurement of a single physiological parameter. The groups of Bruce Jenkins and Marcus Rudin have led pharmacological MRI studies with USPIO. Pharmacological challenges included bicuculline (γ-aminobutyric acid antagonist) (96,99), cocaine (dopamine transporter inhibitor) (23,100–102), dopamine D2/D3 receptor agonists and antagonists (103,104), nicotine (105), *N*-methyl-D-aspartate receptor agonists (106), acetylcholine-esterase inhibitor (107) and amphetamine (dopamine releaser) (108,109).

CONCLUSIONS

CBV mapping with intravascular, long-half-life USPIO offers new imaging approaches for animal research. Although USPIO is not currently approved for human CBV studies, Feraheme (AMAG Pharmaceuticals) is approved for iron deficiency anemia treatments in humans. Thus, the approval of USPIO as a blood pool agent in humans may be possible in the near future. With USPIO, baseline CBV and its changes induced by functional activity and pharmacological intervention can be reliably and easily determined with high sensitivity, even at low magnetic fields. CBV-weighted fMRI provides enhanced sensitivity, reduced large vessel contribution and improved spatial specificity relative to BOLD fMRI, and measures a single physiological parameter, which is easily interpretable.

Acknowledgements

This work was supported by the National Institutes of Health (EB003375, EB003324 and NS44589). We also thank Dr Alex Poplawsky for editorial assistance, Drs Yong Ro Kim and Joseph Mandeville at Massachusetts General Hospital for helpful discussion, Dr Ping Wang for experimental assistance and Drs Tsukasa Nagaoka, Mitshiro Fukuda, Chan-Hong Moon and Xiaopeng Zong for the performance of some CBV studies.

REFERENCES

1. Johnston DL, Liu P, Lauffer RB, Newell JB, Wedeen VJ, Rosen BR, Brady TJ, Okada RD. Use of gadolinium-DTPA as a myocardial perfusion agent: potential applications and limitations for magnetic resonance imaging. J. Nucl. Med. 1987; 28(5): 871–877.
2. Villringer A, Rosen BR, Bellieau JW, Ackerman JL, Lauffer RB, Buxton RB, Chao YS, Wedeen VJ, Brady TJ. Dynamic imaging with lanthanide chelates in normal brain: contrast due to magnetic susceptibility effects. Magn. Reson. Med. 1988; 6: 164–174.
3. Belliveau JW, Kennedy DN, McKinstry RC, Buchbinder BR, Weisskoff RM, Cohen MS, Vevea JM, Brady TJ, Rosen BR. Functional mapping of the human visual cortex by magnetic resonance imaging. Science 1991; 254: 716–719.
4. Rosen BR, Belliveau JW, Buchbinder BR, McKinstry RC, Porkka LM, Kennedy DN, Neuder MS, Fisel CR, Aronen HJ, Kwong KK, Weisskoff RF, Cohen MS, Brady TJ. Contrast agents and cerebral hemodynamics. Magn. Reson. Med. 1991; 19(2): 285–292.
5. Willats L, Calamante F. The 39 steps: evading error and deciphering the secrets for accurate dynamic susceptibility contrast MRI. NMR Biomed 2012; DOI: 10.1002/nbm.2833.
6. Corot C, Robert P, Idee JM, Port M. Recent advances in iron oxide nanocrystal technology for medical imaging. Adv. Drug Deliv. Rev. 2006; 58(14): 1471–1504.
7. Weissleder R, Elizondo G, Wittenberg J, Rabito CA, Bengele HH, Josephson L. Ultrasmall superparamagnetic iron oxide: characterization of a new class of contrast agents for MR imaging. Radiology 1990; 175: 489–493.
8. Yablonskiy DA, Haacke EM. Theory of NMR signal behavior in magnetically inhomogeneous tissues: the static dephasing regime. Magn. Reson. Med. 1994; 32(6): 749–763.
9. Kiselev VG, Posse S. Analytical model of susceptibility-induced MR signal dephasing: effect of diffusion in a microvascular network. Magn. Reson. Med. 1999; 41: 499–509.
10. Ogawa S, Menon RS, Tank DW, Kim SG, Merkle H, Ellermann JM, Ugurbil K. Functional brain mapping by blood oxygenation level-dependent contrast magnetic resonance imaging. A comparison of signal characteristics with a biophysical model. Biophys. J. 1993; 64(3): 803–812.
11. Weisskoff RM, Zuo CS, Boxerman JL, Rosen BR. Microscopic susceptibility variation and transverse relaxation: theory and experiment. Magn. Reson. Med. 1994; 31: 601–610.
12. Boxerman JL, Hamberg LM, Rosen BR, Weisskoff RM. MR contrast due to intravascular magnetic perturbations. Magn. Reson. Med. 1995; 34: 555–566.
13. Dennie J, Mandeville JB, Boxerman JL, Packard SD, Rosen BR, Weisskoff RM. NMR imaging of changes in vascular morphology due to tumor angiogenesis. Magn. Reson. Med. 1998; 40: 793–799.
14. Tropres I, Grimault S, Vaeth A, Grillon E, Julien C, Payen JF, Lamalle L, Decorps M. Vessel size imaging. Magn. Reson. Med. 2001; 45: 397–408.
15. Berry I, Benderbous S, Ranjeva J-P, Gracia-Meavilla D, Manelfe C, Le Bihan D. Contribution of Sinerem used as blood-pool contrast agent: detection of cerebral blood volume changes during apnea in the rabbit. Magn. Reson. Med. 1996; 36: 415–419.
16. Kennan RP, Scanley BE, Innis RB, Gore JC. Physiological basis for BOLD MR signal changes due to neuronal stimulation: separation of blood volume and magnetic susceptibility effects. Magn. Reson. Med. 1998; 40: 840–846.
17. Mandeville JB, Marota JJ, Kosofsky BE, Keltner JR, Weissleder R, Rosen BR, Weisskoff RM. Dynamic functional imaging of relative cerebral blood volume during rat forepaw stimulation. Magn. Reson. Med. 1998; 39(4): 615–624.
18. van Bruggen N, Busch E, Palmer JT, Williams S-P, de Crespigny AJ. High-resolution functional magnetic resonance imaging of the rat brain: mapping changes in cerebral blood volume using iron oxide contrast media. J. Cereb. Blood Flow Metab. 1998; 18: 1178–1183.
19. Mandeville JB, Marota JJA. Vascular filters of functional MRI: spatial localization using BOLD and CBV contrast. Magn. Reson. Med. 1999; 42: 591–598.
20. Mandeville JB, Jenkins BG, Kosofsky BE, Moskowitz MA, Rosen BR, Marota JJA. Regional sensitivity and coupling of BOLD and CBV changes during stimulation of rat brain. Magn. Reson. Med. 2001; 45: 443–447.
21. Mandeville J, Jenkins B, Chen Y, Choi J-K, Kim Y, Belen D, Liu C, Kosofsky B, Marota JJA. Exogenous contrast agent improves sensitivity of gradient-echo functional magnetic resonance imaging at 9.4 T. Magn. Reson. Med. 2004; 52: 1272–1281.
22. Mandeville JB. IRON fMRI measurements of CBV and implications for BOLD signal. NeuroImage 2012; 62: 1000–1006.
23. Chen YC, Mandeville JB, Nguyen TV, Talele A, Cavagna F, Jenkins BG. Improved mapping of pharmacologically induced neuronal activation using the IRON technique with superparamagnetic blood pool agents. J. Magn. Reson. Imaging, 2001; 14(5): 517–524.

24. Shen T, Weissleder R, Papisov M, Bogdanov JA, Brady TJ. Monocrystalline iron oxide nanocompounds (MION): physicochemical properties. Magn. Reson. Med. 1993; 29: 599–604.
25. Wu EX, Tang H, Jensen JH. Applications of ultrasmall superparamagnetic iron oxide contrast agents in the MR study of animal models. NMR Biomed. 2004; 17(7): 478–483.
26. Wagenseil JE, Johansson LO, Lorenz CH. Characterization of T_1 relaxation and blood-myocardial contrast enhancement of NC100150 injection in cardiac MRI. J. Magn. Reson. Imaging 1999; 10(5): 784–789.
27. Weissleder R, Bogdanov A, Neuwelt EA, Papisov M. Long-lasting iron oxides for MR imaging. Adv. Drug Deliv. Rev. 1995; 16: 321–334.
28. Bonnemain B. Superparamagnetic agents in magnetic resonance imaging: physicochemical characteristics and clinical applications. A review. J. Drug Target. 1998; 6(3): 167–174.
29. Vanduffel W, Fize D, Mandeville JB, Nelissen K, van Hecke P, Rosen BR, Tootell RBH, Orban GA. Visual motion processing investigated using contrast agent-enhanced fMRI in awake behaving monkeys. Neuron 2001; 32: 565–577.
30. Leite FP, Tsao D, Vanduffel W, Fize D, Sasaki Y, Wald LL, Dale AM, Kwong K, Orban GA, Rosen B, Tootell RBH, Mandeville JB. Repeated fMRI using iron oxide contrast agent in awake, behaving macaques at 3 Tesla. NeuroImage 2002; 16: 283–294.
31. Li W, Tutton S, Vu AT, Pierchala L, Li BS, Lewis JM, Prasad PV, Edelman RR. First-pass contrast-enhanced magnetic resonance angiography in humans using ferumoxytol, a novel ultrasmall superparamagnetic iron oxide (USPIO)-based blood pool agent. J. Magn. Reson. Imaging 2005; 21(1): 46–52.
32. Bjornerud A, Johansson LO, Briley-Saebo K, Ahlstrom HK. Assessment of T_1 and T_2* effects in vivo and ex vivo using iron oxide nanoparticles in steady state – dependence on blood volume and water exchange. Magn. Reson. Med. 2002; 47(3): 461–471.
33. Zhao F, Wang P, Harel N, Nagaoka T, Kim S-G. Contrast agent-enhanced functional magnetic resonance imaging at 4.7T and 9.4T. *Proceedings of the 11th Annual Meeting ISMRM*, Toronto, ON, Canada, 2003; 1770.
34. Chu SC, Xu Y, Balschi JA, Springer CS Jr. Bulk magnetic susceptibility shifts in NMR studies of compartmentalized samples: use of paramagnetic reagents. Magn. Reson. Med. 1990; 13(2): 239–262.
35. Spees W, Yablonskiy D, Oswood M, Ackerman JH. Water proton MR properties of human blood at 1.5 Tesla: magnetic susceptibility, T_1, T_2, T^*_2, and non-Lorentzian signal behavior. Magn. Reson. Med. 2001; 45: 533–542.
36. Kim T, Masamoto K, Hendrich K, Kim S-G. Arterial versus total blood volume changes during neural activity-induced cerebral blood flow change: implication for BOLD fMRI. J. Cereb. Blood Flow Metab. 2007; 27: 1235–1247.
37. Weisskoff RM, Hoppel BJ, Rosen BR. Signal changes in dynamic contrast studies: theory and experiment *in vivo*. J. Magn. Reson. Imaging 1992; 2: 77.
38. Weisskoff RM, Kiihne S. MRI susceptometry: image-based measurement of absolute susceptibility of MR contrast agents and human blood. Magn. Reson. Med. 1992; 24: 375–383.
39. Kim T, Kim S-G. Quantification of cerebral arterial blood volume and cerebral blood flow using MRI with modulation of tissue and vessel (MOTIVE) signals. Magn. Reson. Med. 2005; 54: 333–342.
40. Anzai Y, Prince MR, Chenevert TL, Maki JH, Londy F, London M, McLachlan SJ. MR angiography with an ultrasmall superparamagnetic iron oxide blood pool agent. J. Magn. Reson. Imaging 1997; 7(1): 209–214.
41. Pathak AP, Rand SD, Schmainda KM. The effect of brain tumor angiogenesis on the in vivo relationship between the gradient-echo relaxation rate change ($DeltaR_2$*) and contrast agent (MION) dose. J. Magn. Reson. Imaging 2003; 18(4): 397–403.
42. Bolan PJ, Yacoub E, Garwood M, Ugurbil K, Harel N. In vivo micro-MRI of intracortical neurovasculature. NeuroImage 2006; 32(1): 62–69.
43. Kim T, Kim S-G. Temporal dynamics and spatial specificity of arterial and venous blood volume changes during visual stimulation: implication for BOLD quantification. J. Cereb. Blood Flow Metab. 2011; 31(5): 1211–1222.
44. Herscovitch P, Raichle ME. What is the correct value for the brain–blood partition coefficient for water? J. Cereb. Blood Flow Metab. 1985; 5: 65–69.
45. Zhao F, Wang P, Hendrich K, Ugurbil K, Kim S-G. Cortical layer-dependent BOLD and CBV responses measured by spin-echo and gradient-echo fMRI: insights into hemodynamic regulation. NeuroImage 2006; 30: 1149–1160.
46. Tieman S, Mollers S, Tieman D, White J. The blood supply of the cat's visual cortex and its postnatal development. Brain Res. 2004; 998(1): 100–112.
47. Le Duc G, Peoc'h M, Remy C, Charpy O, Muller RN, Le Bas JF, Decorps M. Use of T(2)-weighted susceptibility contrast MRI for mapping the blood volume in the glioma-bearing rat brain. Magn. Reson. Med. 1999; 42(4): 754–761.
48. Wu EX, Wong KK, Andrassy M, Tang H. High-resolution in vivo CBV mapping with MRI in wild-type mice. Magn. Reson. Med. 2003; 49 (4): 765–770.
49. Dunn J, Roche M, Springett R, Abajian M, Merlis J, Daghlian C, Lu S, Makki M. Monitoring angiogenesis in brain using steady-state quantification of $DeltaR_2$ with MION infusion. Magn. Reson. Med. 2004; 51: 55–61.
50. Jensen J, Chandra R. MR imaging of microvasculature. Magn. Reson. Med. 2000; 44: 224–230.
51. Tropres I, Lamalle L, Peoch M, Farion R, Usson Y, Decorps M, Remy C. In vivo assessment of tumoral angiogenesis. Magn. Reson. Med. 2004; 51: 533–541.
52. Ungersma SE, Pacheco G, Ho C, Yee SF, Ross J, van Bruggen N, Peale FV Jr, Ross S, Carano RA. Vessel imaging with viable tumor analysis for quantification of tumor angiogenesis. Magn. Reson. Med. 2010; 63(6): 1637–1647.
53. Douma K, Oostendorp M, Slaaf DW, Post MJ, Backes WH, van Zandvoort MA. Evaluation of magnetic resonance vessel size imaging by two-photon laser scanning microscopy. Magn. Reson. Med. 2010; 63(4): 930–939.
54. Kennan RP, Scanley E, Gore JC. Physiological basis for BOLD MR signal changes due to hypoxia/hyperoxia: separation of blood volume and magnetic susceptibility effects. Magn. Reson. Med. 1997; 37: 953–956.
55. Lu H, Scholl CA, Zuo Y, Stein EA, Yang Y. Quantifying the blood oxygenation level dependent effect in cerebral blood volume-weighted functional MRI at 9.4T. Magn. Reson. Med. 2007; 58(3): 616–621.
56. Harel N, Zhao F, Wang P, Kim S-G. Cortical layer specificity of BOLD and CBV fMRI signals at ultra-high resolution. *Proceedings of the 10th Annual Meeting ISMRM*, Honolulu, HI, USA, 2002; 9.
57. Payne BR, Peters A. The concept of cat primary visual cortex. In: Payne BR, Peters A, Editors. *The Cat Primary Visual Cortex*. Academic Press: San Diego; 2002, pp. 1–129.
58. Harel N, Lin J, Moeller S, Ugurbil K, Yacoub E. Combined imaging–histological study of cortical laminar specificity of fMRI signals. NeuroImage, 2006; 29: 879–887.
59. Mandeville JB, Leite FP, Marota JJ. Spin-echo MRI underestimates functional changes in microvascular cerebral blood plasma volume using exogenous contrast agent. Magn. Reson. Med. 2007; 58(4): 769–776.
60. Van Camp N, Peeters RR, Van der Linden A. A comparison between blood oxygenation level-dependent and cerebral blood volume contrast in the rat cerebral and cerebellar somatosensoric cortex during electrical paw stimulation. J. Magn. Reson. Imaging 2005; 22(4): 483–491.
61. Qiu D, Zaharchuk G, Christen T, Ni WW, Moseley ME. Contrast-enhanced functional blood volume imaging (CE-fBVI): enhanced sensitivity for brain activation in humans using the ultrasmall superparamagnetic iron oxide agent ferumoxytol. NeuroImage 2012; 62: 1726–1731.
62. Smirnakis SM, Schmid MC, Weber B, Tolias AS, Augath M, Logothetis NK. Spatial specificity of BOLD versus cerebral blood volume fMRI for mapping cortical organization. J. Cereb. Blood Flow Metab. 2007; 27(6): 1248–1261.
63. Keilholz SD, Silva AC, Raman M, Merkle H, Koretsky AP. BOLD and CBV-weighted functional magnetic resonance imaging of the rat somatosensory system. Magn. Reson. Med. 2006; 55(2): 316–324.
64. Lee SP, Harel N, Nagaoka T, Kim S-G. Quantification of relative CBV changes during neural stimulation. Proc. Int. Soc. Magn. Reson. Med. 2002; 10: 644.
65. Mandeville JB, Marota J, Ayata C, Zaharchuk G, Moskowitz M, Rosen BR, Weisskoff RM. Evidence of a cerebrovascular postarteriole windkessel with delayed compliance. J. Cereb. Blood Flow Metab. 1999; 19: 679–689.
66. Silva AC, Koretsky A, Duyn J. Functional MRI impulse response for BOLD and CBV contrast in rat somatosensory cortex. Magn. Reson. Med. 2007; 57: 1110–1118.
67. Lu H, Soltysik DA, Ward BD, Hyde JS. Temporal evolution of the CBV-fMRI signal to rat whisker stimulation of variable duration and intensity: a linearity analysis. NeuroImage 2005; 26(2): 432–440.

68. Jin T, Kim S-G. Cortical layer-dependent dynamic blood oxygenation, cerebral blood flow and cerebral blood volume responses during visual stimulation. NeuroImage 2008; 43: 1–9.
69. Palmer J, de Crespigny A, Williams S-P, Busch E, van Bruggen N. High-resolution mapping of discrete represenational areas in rat somatosensory cortex using blood volume-dependent functional MRI. NeuroImage 1999; 9: 383–392.
70. Lu H, Patel S, Luo F, Li SJ, Hillard CJ, Ward BD, Hyde JS. Spatial correlations of laminar BOLD and CBV responses to rat whisker stimulation with neuronal activity localized by Fos expression. Magn. Reson. Med. 2004; 52(5): 1060–1068.
71. Zhao F, Wang P, Hendrich K, Kim S-G. Spatial specificity of cerebral blood volume-weighted fMRI responses at columnar resolution. NeuroImage 2005; 27: 416–424.
72. Fukuda M, Moon C-H, Wang P, Kim S-G. Mapping iso-orientation columns by contrast agent-enhanced functional MRI: reproducibility, specificity and evaluation by optical imaging of intrinsic signal. J. Neurosci. 2006; 26: 11 821–11 832.
73. Kim D-S, Duong TQ, Kim S-G. High-resolution mapping of iso-orientation columns by fMRI. Nat. Neurosci. 2000; 3: 164–169.
74. Hubel DH, Wiesel TN. Receptive fields, binocular interaction and functional architecture in the cat's visual cortex. J. Physiol. London 1962; 160: 215–243.
75. Hamberg LM, Boccalini P, Stranjalis G, Hunter GJ, Huang Z, Halpern E, Weisskoff RM, Moskowitz MA, Rosen BR. Continuous assessment of relative cerebral blood volume in transient ischemia using steady state susceptibility-contrast MRI. Magn. Reson. Med. 1996; 35: 168–173.
76. de Crespigny AJ, Rother J, Beaulieu C, Neumann-Haefelin T, Moseley ME. Comparison of diffusion, blood oxygenation, and blood volume changes during global ischemia in rats. Magn. Reson. Med. 2001; 45(1): 10–16.
77. Kim YR, Huang IJ, Lee SR, Tejima E, Mandeville JB, van Meer MP, Dai G, Choi YW, Dijkhuizen RM, Lo EH, Rosen BR. Measurements of BOLD/CBV ratio show altered fMRI hemodynamics during stroke recovery in rats. J. Cereb. Blood Flow Metab. 2005; 25(7): 820–829.
78. Payen JF, Vath A, Koenigsberg B, Bourlier V, Decorps M. Regional cerebral plasma volume response to carbon dioxide using magnetic resonance imaging. Anesthesiology 1998; 88(4): 984–992.
79. Payen JF, Briot E, Tropres I, Julien-Dolbec C, Montigon O, Decorps M. Regional cerebral blood volume response to hypocapnia using susceptibility contrast MRI. NMR Biomed. 2000; 13(7): 384–391.
80. Broux C, Tropres I, Montigon O, Julien C, Decorps M, Payen JF. The effects of sustained hyperventilation on regional cerebral blood volume in thiopental-anesthetized rats. Anesth. Analg. 2002; 95(6): 1746–1751.
81. Julien-Dolbec C, Tropres I, Montigon O, Reutenauer H, Ziegler A, Decorps M, Payen JF. Regional response of cerebral blood volume to graded hypoxic hypoxia in rat brain. Br. J. Anaesth. 2002; 89(2): 287–293.
82. Mandeville JB, Marota JJA, Ayata C, Moskowitz MA, Weisskoff RM, Rosen BR. MRI measurement of the temporal evolution of relative $CMRO_2$ during rat forepaw stimulation. Magn. Reson. Med. 1999; 42: 944–951.
83. Hyder F, Kida I, Behar KL, Kennan RP, Maciejewski PK, Rothman DL. Quantitative functional imaging of the brain: towards mapping neuronal activity by BOLD fMRI. NMR Biomed. 2001; 14: 413–431.
84. Wu G, Luo F, Li Z, Zhao X, Li SJ. Transient relationships among BOLD, CBV, and CBF changes in rat brain as detected by functional MRI. Magn. Reson. Med. 2002; 48(6): 987–993.
85. Shen Q, Ren H, Duong TQ. CBF, BOLD, CBV, and $CMRO_2$ fMRI signal temporal dynamics at 500-msec resolution. J. Magn. Reson. Imaging 2008; 27(3): 599–606.
86. Shih YY, Wey HY, De La Garza BH, Duong TQ. Striatal and cortical BOLD, blood flow, blood volume, oxygen consumption, and glucose consumption changes in noxious forepaw electrical stimulation. J. Cereb. Blood Flow Metab. 2011; 31(3): 832–841.
87. Grubb RL, Raichle ME, Eichling JO, Ter-Pogossian MM. The effects of changes in $PaCO_2$ on cerebral blood volume, blood flow, and vascular mean transit time. Stroke 1974; 5: 630–639.
88. Kida I, Rothman DL, Hyder F. Dynamics of changes in blood flow, volume, and oxygenation: implications for dynamic functional magnetic resonance imaging calibration. J. Cereb. Blood Flow Metab. 2007; 27(4): 690–696.
89. Lee S-P, Duong T, Yang G, Iadecola C, Kim S-G. Relative changes of cerebral arterial and venous blood volumes during increased cerebral blood flow: implications for BOLD fMRI. Magn. Reson. Med. 2001; 45: 791–800.
90. Zong X, Kim T, Kim S-G. Contributions of dynamic venous blood volume versus oxygenation level changes to BOLD fMRI. NeuroImage 2012; 60(4): 2238–2246.
91. Kim T, Kim S-G. Quantification of cerebral arterial blood volume using arterial spin labeling with intravoxel incoherent motion-sensitive gradients. Magn. Reson. Med. 2006; 55: 1047–1057.
92. Kim T, Hendrich K, Kim S-G. Functional MRI with magnetization transfer effects: determination of BOLD and arterial blood volume changes. Magn. Reson. Med. 2008; 60: 1518–1523.
93. Dubowitz D, Bernheim K, Chen D, Bradley W, Andersen R. Enhancing fMRI contrast in awake-behaving primates using intravascular magnetite dextran nanoparticles. Neuroreport 2001; 12: 2335–2340.
94. Durand JB, Nelissen K, Joly O, Wardak C, Todd JT, Norman JF, Janssen P, Vanduffel W, Orban GA. Anterior regions of monkey parietal cortex process visual 3D shape. Neuron 2007; 55(3): 493–505.
95. Tsao DY, Moeller S, Freiwald WA. Comparing face patch systems in macaques and humans. Proc. Natl. Acad. Sci. USA 2008; 105(49): 19 514–19 519.
96. Mueggler T, Baumann D, Rausch M, Rudin M. Bicuculline-induced brain activation in mice detected by functional magnetic resonance imaging. Magn. Reson. Med. 2001; 46(2): 292–298.
97. Zhao F, Williams M, Meng X, Welsh DC, Coimbra A, Crown ED, Cook JJ, Urban MO, Hargreaves R, Williams DS. BOLD and blood volume-weighted fMRI of rat lumbar spinal cord during non-noxious and noxious electrical hindpaw stimulation. NeuroImage 2008; 40(1): 133–147.
98. Zhao F, Williams M, Meng X, Welsh DC, Grachev ID, Hargreaves R, Williams DS. Pain fMRI in rat cervical spinal cord: an echo planar imaging evaluation of sensitivity of BOLD and blood volume-weighted fMRI. NeuroImage 2009; 44(2): 349–362.
99. Reese T, Bjelke B, Porszasz R, Baumann D, Bochelen D, Sauter A, Rudin M. Regional brain activation by bicuculline visualized by functional magnetic resonance imaging. Time-resolved assessment of bicuculline-induced changes in local cerebral blood volume using an intravascular contrast agent. NMR Biomed. 2000; 13(1): 43–49.
100. Chen YI, Famous K, Xu H, Choi JK, Mandeville JB, Schmidt HD, Pierce RC, Jenkins BG. Cocaine self-administration leads to alterations in temporal responses to cocaine challenge in limbic and motor circuitry. Eur. J. Neurosci. 2011; 34(5): 800–815.
101. Mandeville JB, Choi JK, Jarraya B, Rosen BR, Jenkins BG, Vanduffel W. FMRI of cocaine self-administration in macaques reveals functional inhibition of basal ganglia. Neuropsychopharmacology 2011; 36(6): 1187–1198.
102. Perles-Barbacaru TA, Procissi D, Demyanenko AV, Hall FS, Uhl GR, Jacobs RE. Quantitative pharmacologic MRI: mapping the cerebral blood volume response to cocaine in dopamine transporter knockout mice. NeuroImage 2011; 55(2): 622–628.
103. Chen YC, Choi JK, Andersen SL, Rosen BR, Jenkins BG. Mapping dopamine D2/D3 receptor function using pharmacological magnetic resonance imaging. Psychopharmacology (Berlin) 2005; 180(4): 705–715.
104. Choi JK, Mandeville JB, Chen YI, Grundt P, Sarkar SK, Newman AH, Jenkins BG. Imaging brain regional and cortical laminar effects of selective D3 agonists and antagonists. Psychopharmacology (Berlin) 2010; 212(1): 59–72.
105. Choi JK, Mandeville JB, Chen YI, Kim YR, Jenkins BG. High resolution spatial mapping of nicotine action using pharmacologic magnetic resonance imaging. Synapse 2006; 60(2): 152–157.
106. Panizzutti R, Rausch M, Zurbrugg S, Baumann D, Beckmann N, Rudin M. The pharmacological stimulation of NMDA receptors via co-agonist site: an fMRI study in the rat brain. Neurosci. Lett. 2005; 380(1–2): 111–115.
107. Rausch M, Gentsch C, Enz A, Baumann D, Rudin M. A study paradigm allowing comparison of multiple high-resolution rCBV-maps for the examination of drug effects. NMR Biomed. 2005; 18(4): 260–268.
108. Jenkins BG, Sanchez-Pernaute R, Brownell AL, Chen YC, Isacson O. Mapping dopamine function in primates using pharmacologic magnetic resonance imaging. J. Neurosci. 2004; 24(43): 9553–9560.
109. Ren J, Xu H, Choi JK, Jenkins BG, Chen YI. Dopaminergic response to graded dopamine concentration elicited by four amphetamine doses. Synapse 2009; 63(9): 764–772.